

# Liquid-gas coexistence and critical point shifts in size-disperse fluids

Nigel B. Wilding

*Department of Physics, University of Bath, Bath BA2 7AY, United Kingdom*

Moreno Fasolo and Peter Sollich

*Department of Mathematics, King's College London, Strand, London WC2R 2LS, UK*

(Dated: November 7, 2018)

Specialized Monte Carlo simulations and the moment free energy (MFE) method are employed to study liquid-gas phase equilibria in size-disperse fluids. The investigation is made subject to the constraint of *fixed* polydispersity, i.e. the form of the ‘parent’ density distribution  $\rho^0(\sigma)$  of the particle diameters  $\sigma$ , is prescribed. This is the experimentally realistic scenario for e.g. colloidal dispersions. The simulations are used to obtain the cloud and shadow curve properties of a Lennard-Jones fluid having diameters distributed according to a Schulz form with a large ( $\delta \approx 40\%$ ) degree of polydispersity. Good qualitative accord is found with the results from a MFE method study of a corresponding van der Waals model that incorporates size-dispersity both in the hard core reference and the attractive parts of the free energy. The results show that polydispersity engenders considerable broadening of the coexistence region between the cloud curves. The principal effect of fractionation in this region is a common overall scaling of the particle sizes and typical inter-particle distances, and we discuss why this effect is rather specific to systems with Schulz diameter distributions. Next, by studying a family of such systems with distributions of various widths, we estimate the dependence of the critical point parameters on  $\delta$ . In contrast to a previous theoretical prediction, size-dispersity is found to raise the critical temperature above its monodisperse value. Unusually for a polydisperse system, the critical point is found to lie at or very close to the extremum of the coexistence region in all cases. We outline an argument showing that such behaviour will occur whenever size polydispersity affects only the range, rather than the strength of the inter-particle interactions.

PACS numbers: 64.70Fx, 68.35.Rh

## I. INTRODUCTION AND BACKGROUND

A fluid is termed polydisperse when its constituent particles are not all identical, but exhibit continuous variation in some physical attribute ( $\sigma$ , say) such as size, shape, charge etc. The state of the system is then quantifiable in terms of a density distribution  $\rho(\sigma)$ , measuring the number density of particles of each  $\sigma$  [1, 2]. Conventionally, one identifies two distinct classes of polydispersity: *variable* and *fixed*. Variable polydispersity pertains to systems such as ionic micelles, oil-water emulsions and blood [3–7] where the degree of polydispersity (as measured by the form of  $\rho(\sigma)$ ) can change under the influence of external factors such as pressure, temperature or pH. By contrast, for systems exhibiting fixed polydispersity, the relative proportions of particles of different  $\sigma$  are prescribed by the process of their chemical manufacture. Examples in this category include colloidal dispersions, liquid crystals and polymer solutions [8–10]. For such systems, the *shape* of  $\rho(\sigma)$  is constant, only its *scale* can vary depending on the quantity of solvent present.

In the present work we focus our attention on fluids exhibiting fixed polydispersity. A central issue in such systems is the nature of their phase behaviour. It has long been appreciated that this can be considerably more complex than that of monodisperse systems [11]. Indeed, in some cases the presence of polydispersity is predicted to engender completely new phases, such as the cascades of demixing transitions that occur in length-disperse polymers [12] or the splitting of the triple point in polydis-

perse liquid-crystal polymers [13]. But even when polydispersity is not a prerequisite for the existence of a phase transition, (e.g. colloid-solvent demixing in colloids), it can considerably enrich the character of the transition. The reason for this is *fractionation*: at phase coexistence, particles of each  $\sigma$  may partition themselves unevenly between two (or more) coexisting ‘daughter’ phases as long as—due to particle conservation—the overall composition  $\rho^0(\sigma)$  of the ‘parent’ phase is maintained. The consequences of fractionation for phase diagrams can be dramatic. For example, the conventional liquid-gas binodal of a monodisperse system (which connects the ends of tie-lines in a density-temperature diagram) splits into a ‘cloud’ and a ‘shadow’ curve. These give, respectively, the density at which phase coexistence first occurs and the density of the incipient phase. The curves do not coincide because the shadow phase in general differs in composition from the parent. Further fractionation effects are evident when the phase diagram is represented in terms of external fields, such as temperature and pressure. In contrast to monodisperse systems, for which coexistence occurs along a line in the pressure-temperature projection of the phase diagram, in the presence of polydispersity, this line is broadened into a coexistence *region* [14, 15].

Only recently has experimental work started to clarify in a systematic fashion the generic consequences of polydispersity for phase coexistence properties [16–18], and fundamental questions remain unresolved. Consider, for instance, a prototype model comprising a system of

spherical particles exhibiting a short ranged repulsion and a long ranged attraction. Even in such a basic system, polydispersity may be manifest in different forms. The simplest case is that of a purely size-disperse fluid in which the sole variation amongst particles occurs in their diameters. Alternatively the amplitude of interparticle interactions might vary between particles. More realistically, one should almost certainly consider a coupled combination of both size and amplitude polydispersity i.e. the strength with which a particle interacts with a neighbor depends on the sizes of both. To date, however, there is relatively little known about the individual effects of size and amplitude variations in systems exhibiting fixed polydispersity in terms of their influence on phase behaviour. For instance it is unclear just how the liquid-vapor critical temperature and density are affected when polydispersity is introduced into a model; how the critical point shifts depend on the degree and functional form of the polydispersity; what is the extent and nature of fractionation effects in the coexistence region and what is the degree of associated coexistence curve broadening. In view of this, there clearly exists a need for systematic computational and theoretical investigations of liquid-vapor phase behaviour in model polydisperse fluids. In the present paper, we address this need by combining Monte Carlo (MC) simulation and analytical calculations to investigate liquid-gas phase equilibria in size-disperse LJ fluids

As regards previous studies of phase equilibria in polydisperse system, we know of no prior simulation studies of fluids subject to fixed polydispersity (although several have been performed for the variable case [19–22]). Some analytical studies do exist, however, and these typically seek to calculate the system free energy as a function of a set of density variables. Unfortunately, this task is complicated by the fact that the requisite free energy  $f[\rho(\sigma)]$  is a functional of  $\rho(\sigma)$ , and therefore occupies an infinite dimensional space. Consequently the standard tangent plane approach for identifying phase boundaries becomes excessively unwieldy, both conceptually and numerically, and one is normally obliged to resort to approximation schemes [11]. For sufficiently simple model free energies which generalize the van der Waals (vdW) approximation to polydisperse systems, a direct attack on the solution of the phase equilibrium conditions is nevertheless sometimes possible, see e.g. [23, 24]. The reason for this is that such models are normally “truncatable” so that the phase equilibrium conditions can be reduced to nonlinear equations for a finite number of variables (see sec. IV below). This approach has been applied to the study of phase separation in fluids exhibiting separate size and amplitude polydispersity, yielding predictions for the cloud and shadow curves and critical parameters as a function of polydispersity [15].

An approach which more systematically exploits the advantages of truncatable models is the moment free energy method [11, 12]. This approximates the full free energy appropriately in terms of a “moment free energy”

which depends on a small number of density variables, thereby permitting the use of standard tangent plane construction to locate phase boundaries. It thus restores much of the standard geometrical insight to the phase equilibrium analysis, while at the same time being computationally efficient. In particular, the method delivers (for the given free energy) exact results for the location of critical points and the cloud and shadow curves; other aspects of phase coexistence can be calculated within a systematically refinable approximation scheme that eventually allows one to locate the exact solution of the phase equilibrium conditions. The moment free energy has been applied to the study of phase behaviour in systems ranging from polydisperse hard rods to the freezing of hard spheres [11, 25], and we shall deploy it again in the present study.

The paper is arranged as follows [26]. We begin in sec. II by defining the form of the parent density distribution that we have elected to study. Next, in sec. III, we introduce our simulation model and outline the battery of specialized MC techniques necessary to cope with fixed polydispersity and phase coexistence within a grand canonical ensemble framework. The formalism underpinning the MFE method, together with the form of the model free energy to which it has been applied, are described in sec. IV. Turning then to our results, sec. V compares the phase behaviour emerging from the MFE calculations with that determined by the simulations. Finally, sec. VI presents a discussion of our findings and highlights some issues meriting further investigation.

## II. PARENT DISTRIBUTION

We consider systems characterized by a single continuous polydisperse attribute  $\sigma$ , with associated density distribution  $\rho(\sigma)$ . Under conditions of fixed polydispersity, the *shape* of  $\rho(\sigma)$  is imposed. However, its *scale* can vary depending on the amount of solvent present. Following convention, we define a “parent” distribution  $\rho^0(\sigma)$  as

$$\rho^0(\sigma) = n_0 f(\sigma), \quad (1)$$

where  $n_0 = N/V$  is the overall particle number density, while  $f(\sigma)$  is a nominated normalized shape distribution. Since  $\rho^0(\sigma)$  may vary only in terms of its scale  $n_0$ , the system is constrained to traverse a so-called *dilution line* in the full phase space of possible compositions. The value of  $n_0$  thus serves to parameterize this line.

The term “parent” is adopted to emphasize the fact that although (for a given point on the dilution line) the density distribution is fixed globally, the system might nevertheless phase separate into coexisting “daughter” phases whose density distributions differ from the parent. The daughter phase distributions are then related to the parent via a simple volumetric average:

$$x^{(1)}\rho^{(1)}(\sigma) + x^{(2)}\rho^{(2)}(\sigma) = \rho^0(\sigma) \quad (2)$$

where  $Vx^{(1)}$  and  $Vx^{(2)}$  are the volumes of phases (1) and (2) respectively, with  $V$  the sample volume. Note that on the cloud curve marking the onset of phase coexistence, the volume fraction of the incipient (shadow) phase is negligible and thus the density distribution of the cloud phase coincides with that of the parent.

In this work, we will principally be concerned with unimodal shape distributions of the Schulz form:

$$f(\sigma) = \frac{1}{z!} \left( \frac{z+1}{\bar{\sigma}} \right)^{z+1} \sigma^z \exp \left[ - \left( \frac{z+1}{\bar{\sigma}} \right) \sigma \right]. \quad (3)$$

Here  $\bar{\sigma} \equiv 1$  is the average particle diameter, while  $z$  is a parameter controlling the width of the distribution and hence the dimensionless degree of polydispersity. The latter is conventionally defined as the standard deviation of  $\rho(\sigma)$ , normalized by the mean:

$$\delta = \frac{\sqrt{\langle (\sigma - \bar{\sigma})^2 \rangle}}{\bar{\sigma}}. \quad (4)$$

### III. SIMULATION ASPECTS

Possibly the simplest MC simulation strategy for obtaining the thermodynamic properties of a polydisperse fluid is to populate a simulation box of fixed volume  $V$  with an appointed number of particles  $N$  whose sizes are drawn from the desired  $\rho^0(\sigma)$  [27]. Operationally, however, use of such a canonical ensemble is far from optimal because it only samples a single realization of the possible configurations of particle sizes. Moreover the fixed overall particle number prevents effective study of phase separation phenomena.

Experience with the simulation of monodisperse fluids has shown that use of the grand canonical ensemble (GCE) is highly effective for studying fluid phase transitions [28–30]. Its application in the context of polydisperse fluids retains the benefits of the monodisperse case. Moreover, it provides the key to improved sampling of the density distribution  $\rho(\sigma)$ . This is because  $\rho(\sigma)$  can fluctuate *as a whole*, thus capturing many different individual realization of the ensembles of particle sizes and hence catering naturally for fractionation effects. Notwithstanding these advantages, however, the GCE might appear (at first sight) unsuitable for the purpose of traversing a dilution line. This is because the ensemble averaged density distribution  $\bar{\rho}(\sigma)$  ostensibly lies out-with the direct control of the simulator, its form being instead determined by the imposed chemical potential distribution  $\mu(\sigma)$ . Nevertheless, as we have shown previously [31], it turns out to be possible to adapt  $\mu(\sigma)$  in such a way as to realize a specific desired form of  $\rho(\sigma)$  for any temperature of interest. By complementing this approach with extended sampling MC techniques, phase coexistence properties can be studied along a dilution

line. The remainder of this section describes the necessary techniques and the strategy for their implementation.

#### A. Model and algorithm

We consider a fluid of particles interacting via a pairwise potential of the Lennard-Jones (LJ) form:

$$U(r_{ij}, \sigma_{ij}) = 4\epsilon \left[ \left( \frac{\sigma_{ij}}{r_{ij}} \right)^{12} - \left( \frac{\sigma_{ij}}{r_{ij}} \right)^6 \right], \quad (5)$$

with  $\sigma_{ij} = (\sigma_i + \sigma_j)/2$ . A cutoff was applied to the potential for particle separations  $r_{ij} > 2.5\sigma_{ij}$ . The polydispersity enters solely through the continuous distribution of diameters  $\sigma_i$ , which were assigned the Schulz form Eq. (3).

The GCE Monte Carlo algorithm employed to study this model invokes four types of operation: particle displacements, deletions, insertions, and resizing. The particle diameter  $\sigma$  is treated as a continuous variable in the range  $0 \leq \sigma \leq \sigma_c$ , with  $\sigma_c$  a cutoff which we choose as  $\sigma_c = 3$  unless otherwise specified. However, distributions defined on  $\sigma$  such as the instantaneous density  $\rho(\sigma)$ , and the chemical potential  $\mu(\sigma)$ , are represented as histograms defined by discretising the permitted range of  $\sigma$  into 120 bins. For further details concerning the simulation algorithm, as well as the structure, storage and acquisition of data, we refer the interested reader to ref. [31].

The primary observables with which we shall be concerned are the instantaneous density distribution  $\rho(\sigma)$  and its ensemble averaged form  $\bar{\rho}(\sigma)$ . We also accumulate the distribution of several quantities which do not depend explicitly on  $\sigma$ . These are the fluctuating overall number density  $p(n)$ , where  $n = \int d\sigma \rho(\sigma)$ , the distribution of the fluctuating volume fraction  $p(\eta)$ , with  $\eta = (\pi/6) \int d\sigma \sigma^3 \rho(\sigma)$ , and the distributions of the configurational energy  $p(E)$  and the energy per particle  $p(u)$  with  $u = E/N$ .

For simulations of fixed polydispersity at some given temperature  $T$ , one requires that form of the chemical potential distribution  $\mu(\sigma)$  for which  $\bar{\rho}(\sigma)$  matches some target, namely the prescribed parent  $\rho^0(\sigma)$ . The task of determining the desired  $\mu(\sigma)$  is complicated by the fact that it is an unknown *functional* of the parent (i.e.  $\mu(\sigma) = \mu[\rho^0(\sigma)]$ ). Recently, however, a computational tool has been developed that efficiently overcomes this difficulty. The non-equilibrium potential refinement (NEPR) scheme [32] enables the efficient iterative determination of  $\mu[\rho^0(\sigma), T]$ , from a single simulation run, and without the need for an initial guess of its form. To achieve this,  $\mu(\sigma)$  is continually updated (in the course of a simulation run) in such a way as to minimize the deviation of the instantaneous density distribution  $\rho(\sigma)$  from the desired parent form. This procedure realizes a non-equilibrium steady state for which  $\bar{\rho}(\sigma) = \rho^0(\sigma)$ .

However, since tuning  $\mu(\sigma)$  ‘on-the-fly’ in this manner violates detailed balance, the form of  $\mu(\sigma)$  thus obtained is not the equilibrium solution one actually seeks. Nevertheless by performing a series of iterations in which the degree of modification made to  $\mu(\sigma)$  at each step is successively reduced, one can drive the system towards equilibrium, thereby obtaining the correct  $\mu[\rho^0(\sigma), T]$ .

Notwithstanding the utility of the NEPR method for solving the inverse problem  $\mu[\rho^0(\sigma)]$ , its deployment to determine the form of  $\mu(\sigma)$  all along a dilution line would represent a considerable computational endeavor. Fortunately, however, this is not necessary. A single application of the NEPR method, to obtain  $\mu(\sigma)$  at a state point on the dilution line close to the region of interest, suffices to bootstrap an efficient tracking procedure based on Histogram Extrapolation [33] (HE) techniques. Use of HE permits a stepwise exploration of the dilution line to lower or higher densities. The essential idea is to statistically reweight the data for  $\bar{\rho}(\sigma)$  measured at some dilution line point (given by the value of  $n_0$ ) in order to estimate the form of  $\mu(\sigma)$  corresponding to some other not-too-distant value of  $n_0 = n'_0$ . This is achievable, within the HE scheme, by minimizing a cost function measuring the deviation of the extrapolated form of  $\bar{\rho}(\sigma)[\mu(\sigma)]$  from a target corresponding to the desired parent  $n'_0 f(\sigma)$ . Full details of the tracking procedure can be found in ref. [31].

## B. Coexistence curve mapping strategy

Simulation studies of phase coexistence present distinctive computational challenges. Principal among these is the large free energy (surface tension) barrier separating the coexisting phases. In order to accurately locate coexistence points, a sampling scheme must be utilized which enables this barrier to be surmounted [34]. One such scheme is multicanonical preweighting [35], which utilizes a weight function in the MC acceptance probabilities, in order to encourage the simulation to sample the interfacial configurations of low probability. At a given coexistence state point, the requisite weight function takes the form of an approximation to the inverse of the distribution of the fluctuating number density,  $p(n)$ . While specialized techniques allow determination of  $p(n)$  from scratch, in situations where one wishes to track a fluid-fluid phase boundary prior determination of a weight function is unnecessary, provided one commences from the vicinity of the critical point where the barrier to inter-phase crossings is small [30]. Data accumulated here can be used (together with HE) to provide estimates of suitable multicanonical weight functions at lower temperatures [28] where the barrier height is greater.

We seek the intersection of the dilution line with the temperature dependent coexistence region. The latter is delineated by the cloud curves which herald the onset of coexistence when approached from the respective pure phases. The cloud curves (and their corresponding

shadow curves) were obtained as follows. The dilution line tracking procedure was bootstrapped at a gas phase state point on the dilution line at a moderately low temperature by using the NEPR method [32] to determine the form of  $\mu(\sigma)$ . Starting from this point, the dilution line was then followed towards increasing density (with the aid of HE) until the gas spontaneously liquefied. Having estimated the location of a coexistence state point in this manner, the temperature was increased in steps (whilst remaining on the dilution line) until the density difference between the gas and the spontaneously formed liquid vanished, signalling the proximity of the critical point. Finite-size scaling methods [28] were then used to furnish more precise estimates for the critical parameters.

Having located the critical point, a detailed mapping of the cloud and shadow curves was performed. The key to achieving this is the form of the fluctuating overall number density,  $p(n)$ . The gas phase cloud point (incipient liquid phase) corresponds to the situation where  $p(n)$  is bimodal, but with vanishingly small weight in the liquid peak. Under these conditions, the position of the low density gas peak provides an estimate of the gas phase cloud density, while that of the liquid peak gives the liquid shadow density. The converse is true for the liquid phase cloud point and its gas shadow. Determining the cloud and shadow points as a function of temperature yields the cloud and shadow curves. One tracks the gas and liquid cloud curves (and their shadows) in a stepwise fashion downwards in temperature from the critical point, using HE to negotiate each temperature step. HE yields estimates not only for the form of  $\mu(\sigma)$  on the cloud curve at the next temperature, but also the requisite multicanonical weight function. It should be pointed out that while the positions of the peaks in  $p(n)$  provide an accurate estimate of cloud and shadow points at low temperatures, this breaks down near the critical point due to finite-size effects [28]. Thus a naive extrapolation of our curves to their intersection point will tend to overestimate the critical temperature. However, our independent determination of the critical point using finite-size scaling methods is considerably more accurate.

In order to explore the coexistence region one must traverse the dilution line connecting the cloud points at some desired subcritical temperature. The strategy for doing so commences at one cloud point and entails constructing a series of simulations in which the value of  $n_0$  is successively increased. The requisite multicanonical weight function for each simulation state point is again found with the help of HE from the previous state point.

## IV. MOMENT FREE ENERGY METHOD

### A. Model

To describe our system theoretically, we need a suitable free energy; this is a functional of the density distribution  $\rho(\sigma)$  and an ordinary function of temperature. The free

energy (density) of a polydisperse system can generally be decomposed as

$$f = \int d\sigma \rho(\sigma) [\ln \rho(\sigma) - 1] + f^{\text{ex}} \quad (6)$$

where the first part is the free energy of an ideal polydisperse mixture. To find a suitable model the excess free energy  $f^{\text{ex}}$ , we approximate the repulsive part of our LJ interaction as completely hard. For the corresponding contribution to  $f^{\text{ex}}$  we use the BMCSL approximation  $f_{\text{BMCSL}}^{\text{ex}}$  [1, 36, 37]. In the monodisperse case this reproduces the Carnahan-Starling equation of state [38]; in the general polydisperse case it is a function of the moments up to third order of the density distribution,  $\rho_i = \int d\sigma \sigma^i \rho(\sigma)$  ( $i = 0 \dots 3$ ). We then treat the *attractive* part of the interaction potential in the simplest possible way, by adding a quadratic van der Waals term to  $f^{\text{ex}}$ . Using the fact that the interaction volume of two particles of diameters  $\sigma$  and  $\sigma'$  scales as  $(\sigma + \sigma')^3$ , this gives for the overall excess free energy

$$f^{\text{ex}} = f_{\text{BMCSL}}^{\text{ex}} - \frac{1}{2t} \int d\sigma d\sigma' \rho(\sigma) \rho(\sigma') (\sigma + \sigma')^3 \quad (7)$$

$$= f_{\text{BMCSL}}^{\text{ex}} - \frac{1}{t} (\rho_0 \rho_3 + 3\rho_1 \rho_2) \quad (8)$$

where  $t$  is an appropriate dimensionless temperature. We note in this context that for our theoretical calculations we measure all diameters in units of  $\bar{\sigma}$ , all densities in units of the inverse volume of a reference particle,  $1/[(\pi/6)\bar{\sigma}^3]$  and all energies in units of  $k_B T$ . The free energy densities in Eq. (6) and Eq. (8), for example, are in units of  $k_B T/[(\pi/6)\bar{\sigma}^3]$ . Also,  $\rho_3$  is just the volume fraction of particles, while  $\rho_0$  is a scaled number density,  $\rho_0 = (\pi/6)\bar{\sigma}^3 n$ . With these conventions, the BMCSL contribution to the excess free energy takes the form

$$f_{\text{BMCSL}}^{\text{ex}} = \left( \frac{\rho_2^3}{\rho_3^2} - \rho_0 \right) \ln(1 - \rho_3) + \frac{3\rho_1 \rho_2}{1 - \rho_3} + \frac{\rho_2^3}{\rho_3(1 - \rho_3)^2}.$$

Given the approximate character of our model free energy, it would not make sense to try to scale the temperature parameter  $t$  precisely to the temperature in the simulations. Our main aim is to study whether our  $f^{\text{ex}}$  can reproduce the qualitative trends observed in the simulations. While still somewhat crude, our  $f^{\text{ex}}$  is better suited to this task than previous versions [15] because it incorporates polydispersity not only into the attractive contribution, but also into the hard core reference system.

## B. Moment free energy

Our computational approach for determining the phase behaviour of the model defined by Eq. (8) is based on the moment free energy (MFE) method. We give a brief outline here; details can be found in [11, 12, 39, 40]. The

important feature of our excess free energy is that it is *truncatable*, i.e. depends only on a finite set of moments  $\rho_i = \int d\sigma w_i(\sigma) \rho(\sigma)$  defined by weight functions  $w_i(\sigma)$ ; in our case  $w_i(\sigma) = \sigma^i$ . In coexisting phases, the chemical potentials  $\mu(\sigma)$  and pressure  $P$  must be equal. The former are, by differentiation of Eq. (6),

$$\mu(\sigma) = \frac{\delta f}{\delta \rho(\sigma)} = \ln \rho(\sigma) + \sum_i \mu_i^{\text{ex}} w_i(\sigma), \quad \mu_i^{\text{ex}} = \frac{\partial f^{\text{ex}}}{\partial \rho_i} \quad (9)$$

while the pressure is given by the Gibbs-Duhem relation

$$P = -f + \int d\sigma \mu(\sigma) \rho(\sigma) = \rho_0 - f^{\text{ex}} + \sum_i \mu_i^{\text{ex}} \rho_i \quad (10)$$

To the conditions of equality of chemical potentials and pressure we need to add the requirement of conservation of particle number for each species  $\sigma$ , which reads

$$\sum_{\alpha} x^{(\alpha)} \rho^{(\alpha)}(\sigma) = \rho^0(\sigma) \quad (11)$$

where  $\alpha = 1, \dots, p$  labels the phases (compare equation Eq. (2)). One then finds from equality of the  $\mu(\sigma)$ , Eq. (9), together with particle conservation Eq. (11) that the density distributions in coexisting phases can be written as

$$\rho^{(\alpha)}(\sigma) = \rho^0(\sigma) \frac{\exp \left[ \sum_i \lambda_i^{(\alpha)} w_i(\sigma) \right]}{\sum_{\beta} x^{(\beta)} \exp \left[ \sum_i \lambda_i^{(\beta)} w_i(\sigma) \right]} \quad (12)$$

Here the  $\lambda_i^{(\alpha)}$  must obey

$$\lambda_i^{(\alpha)} = -\mu_i^{(\alpha), \text{ex}} + c_i \quad (13)$$

and the  $c_i$  are undetermined constants that do not affect the density distributions Eq. (12). One can fix them e.g. by requiring all the  $\lambda_i^{(\alpha)}$  in one of the phases to be zero. A little reflection then shows that Eq. (13) together with  $\sum_{\alpha} x^{(\alpha)} = 1$  and the equality of the pressures Eq. (10) in all phases give a closed system of nonlinear equations for the  $p(M+1)$  variables  $\lambda_i^{(\alpha)}$  and  $x^{(\alpha)}$ . A solution can thus, in principle, be found by a standard algorithm such as Newton-Raphson. Generating an initial point from which such an algorithm will converge, however, is still a nontrivial problem, especially when more than two phases coexist and/or many moments  $\rho_i$  are involved. Furthermore, the nonlinear phase equilibrium equations permit no simple geometrical interpretation or qualitative insight akin to the construction of phase diagrams from the free energy surface of a finite mixture.

The moment free energy addresses these two disadvantages. To construct it, one starts by modifying the free energy decomposition Eq. (6) to

$$f = \int d\sigma \rho(\sigma) \left[ \ln \frac{\rho(\sigma)}{R(\sigma)} - 1 \right] + f^{\text{ex}}(\{\rho_i\}) \quad (14)$$

In the first (ideal) term, a normalizing factor  $R(\sigma)$  has been included inside the logarithm. This has no effect on the exact thermodynamics because it contributes only terms linear in  $\rho(\sigma)$ , but will play a central role below. One can now argue that the most important moments to treat correctly in the calculation of phase equilibria are those that actually appear in the excess free energy  $f^{\text{ex}}(\{\rho_i\})$ . Accordingly, one imposes particle conservation Eq. (11) only for the  $\rho_i$ , but allows it to be violated in other details of the density distribution  $\rho(\sigma)$  which do not affect the  $\rho_i$ . These “transverse” degrees of freedom are instead chosen to minimize the free energy Eq. (14), and more precisely its ideal part since the excess contribution is a constant for fixed values of the  $\rho_i$ . This minimization gives

$$\rho(\sigma) = R(\sigma) \exp \left[ \sum_i \lambda_i w_i(\sigma) \right] \quad (15)$$

where the Lagrange multipliers  $\lambda_i$  are chosen to give the desired values of the moments

$$\rho_i = \int d\sigma w_i(\sigma) R(\sigma) \exp \left[ \sum_j \lambda_j w_j(\sigma) \right] \quad (16)$$

The corresponding minimum value of  $f$  as given in Eq. (14) then defines the *moment free energy* (MFE)

$$f_{\text{mom}}(\{\rho_i\}) = \left( \sum_i \lambda_i \rho_i - \rho_0 \right) + f^{\text{ex}}(\{\rho_i\}) \quad (17)$$

Since the Lagrange multipliers are (at least implicitly) functions of the moments, the MFE depends only on the  $\rho_i$ . These can now be viewed as densities of “quasi-species” of particles, allowing for example the calculation of moment chemical potentials [12]

$$\mu_i = \frac{\partial f_{\text{mom}}}{\partial \rho_i} = \lambda_i + \frac{\partial f^{\text{ex}}}{\partial \rho_i} = \lambda_i + \mu_i^{\text{ex}} \quad (18)$$

and the corresponding pressure  $P = \sum_i \mu_i \rho_i - f_{\text{mom}}$  which turns out to be identical to the exact expression Eq. (10). A finite-dimensional phase diagram can thus be constructed from  $f_{\text{mom}}$  according to the usual tangency plane rules, ignoring the underlying polydisperse nature of the system. Obviously, though, the results now depend on  $R(\sigma)$ . To understand its influence, one notes that the MFE is simply the free energy of phases in which the density distributions  $\rho(\sigma)$  are of the form Eq. (15). To ensure that the parent phase is contained in the family, one normally chooses its density distribution as the prior,  $R(\sigma) = \rho^0(\sigma)$ ; the MFE procedure will then be exactly valid whenever the density distributions actually arising in the various coexisting phases are members of the corresponding family

$$\rho(\sigma) = \rho^0(\sigma) \exp \left[ \sum_i \lambda_i w_i(\sigma) \right] \quad (19)$$

It is easy to show from Eq. (12) that this condition holds whenever all but one of a set of coexisting phases are of infinitesimal volume compared to the majority phase. Accordingly, the MFE yields *exactly* the onset of phase of coexistence, conventionally represented via cloud and shadow curves as discussed above. Similarly, one can show that spinodals and critical points are found exactly [12].

For coexistence involving finite amounts of different phases the MFE only gives approximate results, since different density distributions from the family Eq. (19), corresponding to two (or more) phases arising from the same parent  $\rho^0(\sigma)$ , do not in general add to recover the parent distribution itself. Moreover, from Gibbs’ phase rule, a MFE depending on  $M$  moments will not predict more than  $M + 1$  coexisting phases, while we know that a polydisperse system can in principle separate into an arbitrary number of phases. Both of these shortcomings can be overcome by including extra moments within the MFE; this systematically increases the accuracy of any calculated phase splits [12]. By choosing the weight functions of the extra moments adaptively, the properties of the coexisting phases can then be predicted with in principle arbitrary accuracy [12, 41]. Importantly for us, the results can in fact be used as initial points from which a solution of the *exact* phase equilibrium problem can be converged successfully [42, 43]. This is the technique that we use here to obtain results in the coexistence region.

## V. RESULTS

Here we report the results of applying the simulation and MFE methods described in sec. III and IV to obtain the phase behaviour of size disperse fluids. Our findings are separated into two parts, those for the sub critical region (sec. V A) and those for the critical region (secs. V B and V C). With regard to the representation of results, the MFE calculations are essentially exact for the given model free energy; symbols indicate the temperatures at which individual calculations were performed and lines are merely guides to the eye. For the simulation results, unless otherwise indicated, statistical errors do not exceed the symbol sizes. Again, lines are guides to the eye.

### A. The subcritical region

Computational complexity limits our investigation of liquid-gas coexistence to the case of a fluid described by a size distribution of the Schulz form, Eq. (3) having width parameter  $z = 5$ . This choice of  $z$  corresponds to a rather large ( $\delta = 40.7\%$ ) degree of polydispersity. In both the simulations and the MFE calculation,  $f(\sigma)$  was truncated at  $\sigma_c = 3.0$  and renormalized appropriately. The simulations were all performed using a simulation box of volume  $V = 11390\bar{\sigma}^3$ . In what follows we quote

all simulation quantities in the standard dimensionless LJ units (e.g.  $t = k_B T / 4\epsilon$ ).

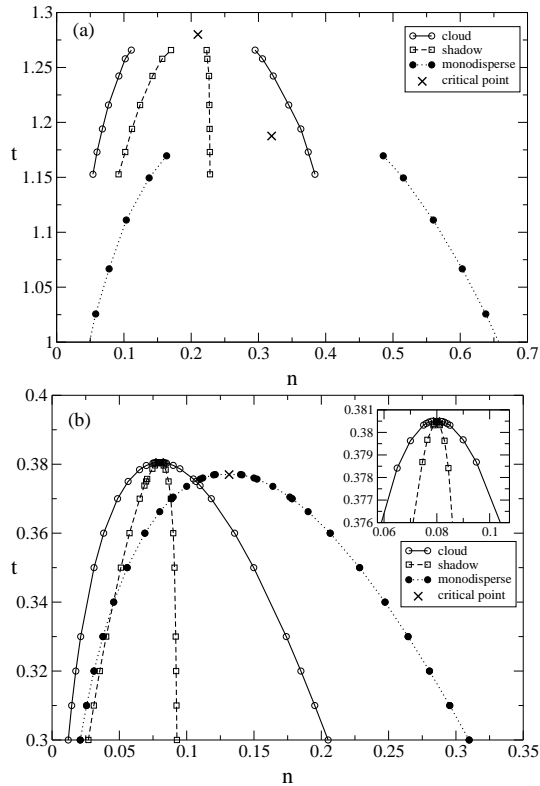


FIG. 1: (a) Cloud and shadow curves in the  $n - T$  plane, as obtained from the simulations. (b) The corresponding prediction of the MFE calculations for a van der Waals model. Also shown for comparison in each case is a portion of the coexistence binodal for the monodisperse limit.

We commence by presenting (in fig. 1) a comparison of the simulation measurements of the cloud and shadow curves in the  $n - t$  projection, with those of the MFE calculations. Apparent in this representation is a stark separation of the cloud and shadow curves. Furthermore, the whole phase diagram is considerably shifted with respect to that of the monodisperse fluid (itself determined previously in the case of fig. 1(a) in ref. [28]). Specifically, one observes that the critical point occurs at a considerably higher temperature than in the monodisperse limit. We note that this particular finding contrasts with that of a previous theoretical study of a size-disperse van der Waals fluid [15], which predicts a *suppression* of the critical temperature with respect to the monodisperse limit.

The order of cloud and shadow curves commonly observed with increasing density in many polydisperse systems (see e.g. [44]) is cloud-shadow-cloud-shadow. By contrast, the order shown in fig. 1 is cloud-shadow-shadow-cloud. Interestingly, however, the order reverts to the standard pattern if one plots the data in terms of the volume fraction  $\eta = (\pi/6) \int d\sigma \sigma^3 \rho(\sigma)$ , rather than the overall number density, as shown in fig. 2. Moreover, one sees that in the  $\eta - t$  representation the differences be-

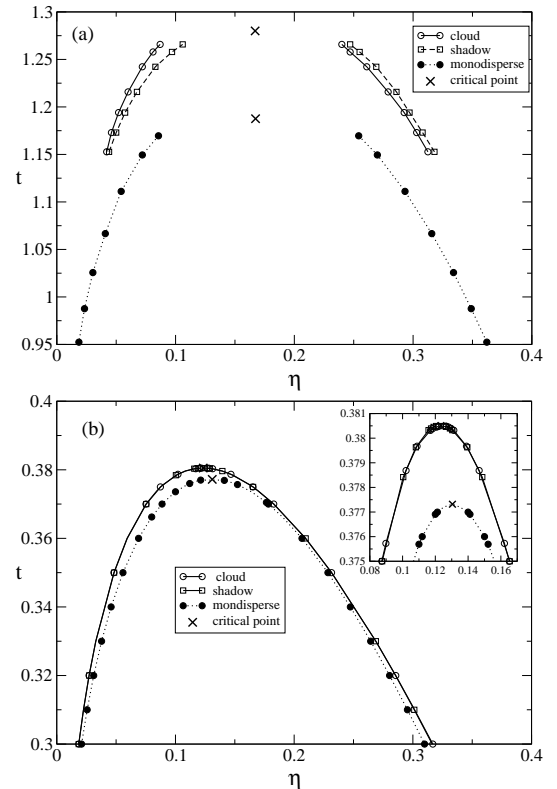


FIG. 2: (a) The simulation, and (b) MFE data of fig. 1, both re-expressed in terms of the volume fraction  $\eta = (\pi/6) \int d\sigma \sigma^3 \rho(\sigma)$ .

tween cloud and shadow phase properties become much less pronounced. This is particularly evident in the MFE results, fig. 2(b), for which the cloud and shadow curves almost coincide, though a close inspection reveals that they are in fact distinct and occur in the same order as observed in the simulations. Similar findings pertain to the energy per particle measured in the cloud and shadow phases (fig. 3), though the qualitative agreement in the shape of the curves between simulations and theory is less good here. One reason for this that in our model free energy the repulsive interactions, which are modelled as hard, do not contribute to the energy  $u$ . In the MFE calculations we therefore determine  $u$  as the value of the attractive van der Waals term from (Eq. 8). In the simulations, on the other hand, both attractive and repulsive interactions contribute to the measured value of  $u$ .

With regard to the critical point parameters, we note that while the critical number density of the polydisperse fluid is considerably less than its value in the monodisperse limit, the simulation estimates of the critical volume fraction for the mono- and polydisperse fluid agree to within error. Moreover, in both the simulations and the MFE results, the critical point is located at or at least extremely close to the maximum of the cloud and shadow curves. We see no evidence for portions of the cloud or shadow curves lying above the critical temper-

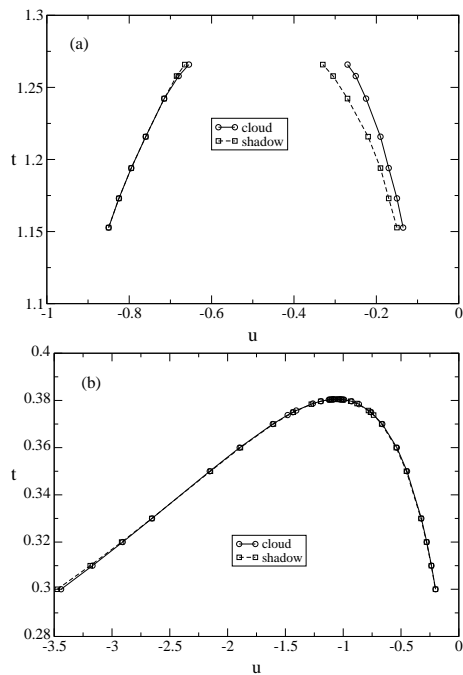


FIG. 3: The energy per particle on the cloud and shadow curves as a function of temperature as obtained from (a) the simulations and (b) the MFE calculation.

ature, which would generically be expected for polydisperse systems [11]. We postpone further discussion of these observations to sec. V C.

Not all distinctions between cloud and shadow curves can be disguised by simply recasting the data in terms of  $\eta$ , rather than  $n$ . At temperatures significantly below criticality, we observe considerable broadening of the coexistence curve in the space of  $\mu(\sigma)$ . This is evident in fig. 4 which shows the form of  $\mu(\sigma)$  at the respective cloud points (marking the boundaries of the two phase region) for the lowest temperature studied in the simulations,  $t = 0.91t_c$ . Such broadening does not occur in monodisperse systems—coexistence occurs at a single value of the chemical potential, not a range of values. The effect is surprisingly large, notwithstanding the high degree of polydispersity of the parent. Indeed, in simulation terms the respective cloud points are so far separated in phase space that to connect them directly (via a route crossing the phase boundary) required some twenty overlapping simulations—three times the number required to connect the cloud point to the critical point at this temperature.

Turning to the form of the density distributions in the shadow phases, an example of the scale of the difference between these and the parent is given in fig 5 for  $t = 0.91t_c$ . The data show that at the gas phase cloud point, larger particles preferentially occupy the liquid shadow phase. Conversely at the liquid phase cloud point, there is a predominance of smaller particles in the gas shadow phase. Clearly the scale of these fractionation effects is significant. We note that the principal fractionation effect is a change in the mean particle di-

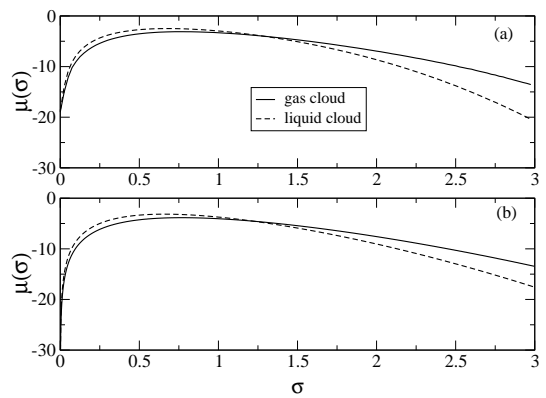


FIG. 4: The form of the chemical potential distribution  $\mu(\sigma)$  at the gas phase and liquid phase cloud points at  $t = 0.91t_c$ . (a) Simulation. (b) MFE calculations.

ameter. The simulations give for the mean diameter in the liquid shadow [45]  $\langle\sigma\rangle = 1.167(3)$ , while in the gas shadow it is  $\langle\sigma\rangle = 0.863$ , both to be compared to that of the parent,  $\langle\sigma\rangle = \bar{\sigma} = 1$ . The changes in the shape of the distribution (as indicated by polydispersities of the shadow phases), are rather smaller. For this temperature ( $t = 0.91t_c$ ), we find in the simulations  $\delta \approx 43\%$  for the liquid shadow, and  $\delta \approx 38.5\%$  for the gas shadow, to be compared with a parent polydispersity of  $\delta = 40.7\%$ .

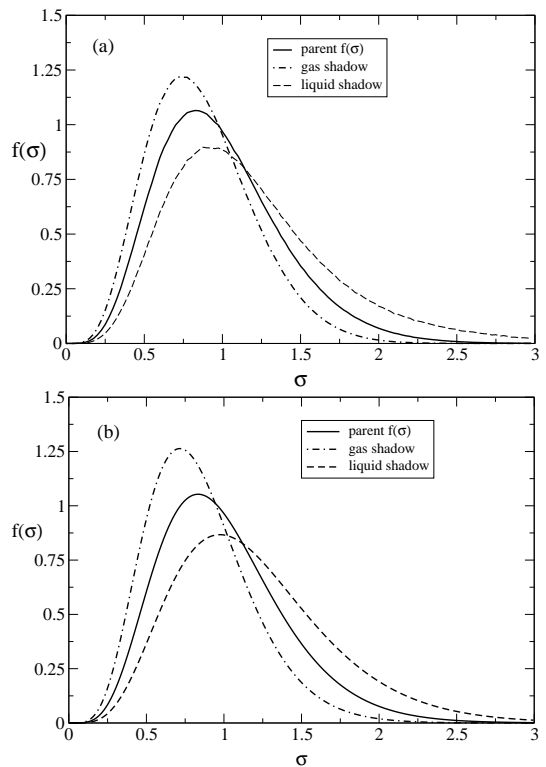


FIG. 5: (a) Simulation estimates of the normalized daughter phase density distributions on the shadow curves at  $t = 0.91t_c$ . Also shown for comparison is the parent distribution. (b) The corresponding results of the MFE calculations.



The temperature dependence of the mean particle size and degree of polydispersity  $\delta$  are shown in fig. 6. It is interesting to note that while the value of  $\delta$  for the liquid shadow initially increases strongly with decreasing temperature, on further reducing temperature it subsequently bends back to lower values of  $\delta$ . (Analogous non-monotonic behaviour is observed in the gas shadow.) Our data (in conjunction with Eq. (4)) show that the origin of this effect lies in the fact that while  $\langle\sigma\rangle$  increases monotonically with decreasing temperature, the standard deviation of the size distribution in the liquid shadow phase first increases strongly as  $t$  is lowered from its critical value, but then saturates to a constant value for temperatures below about  $0.9t_c$ .

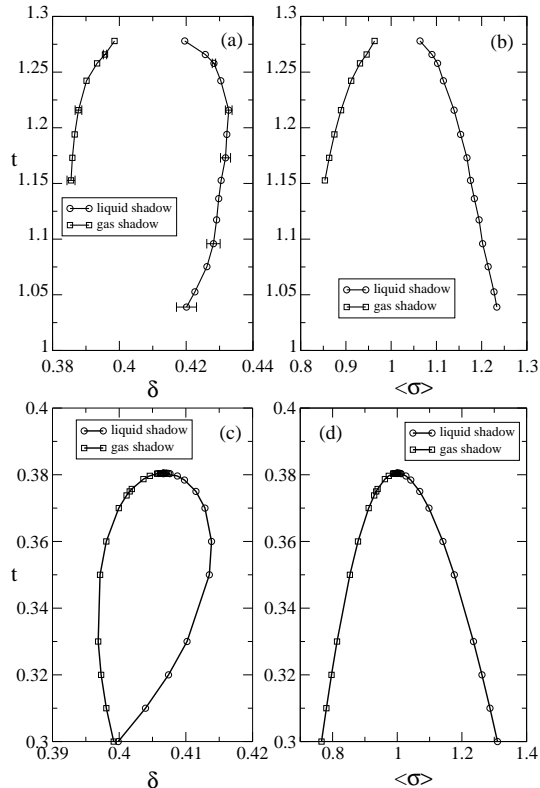


FIG. 6: Simulation estimates of the degree of polydispersity (a) and the mean particle diameter (b) on the shadow curves. (c,d) The corresponding results of the MFE calculations.

In order to explore the coexistence region separating the cloud curves, we have scanned the dilution line at  $t = 0.91t_c$ . The simulations yield the distribution of the fluctuating number density  $p(n)$ , the form of which is shown in fig. 7 for a selection of values of  $n_0$  spanning the coexistence region. One observes that in addition to a transfer of weight between the gas and liquid phase peaks as  $n_0$  is increased from its value at the gas phase cloud point, both the densities of the gas and liquid peaks shift markedly. This shift of course reflects the non-coincidence of the cloud and shadow densities for a given phase. We note further (fig. 8) that the density shifts are non-linear in  $n_0$  and that the overall shift

in the liquid phase density is considerably greater than that for the gas phase.

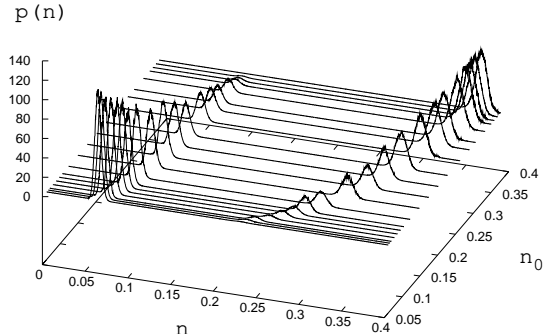


FIG. 7: Distribution of the fluctuating number density  $p(n)$  at a selection of values of the parent density  $n_0$  between the cloud points at  $t = 0.91t_c$ .

Finally in this section, we plot in fig. 9 the measured form of  $p(n)$  for state points spanning the coexistence region, expressed on a logarithmic scale. This representation exposes the magnitude of the surface tension barrier separating the coexisting phases, which is proportional to the logarithm of the peak to trough ratio of the respective distributions [46]. One observes that the surface tension of the liquid shadow at the gas phase cloud point is considerably less than that of the gas shadow at the liquid phase cloud point. This finding reflects the fact that the liquid shadow comprises particles that are on average larger than those of both the parent (cf. fig. 5) and the gas shadow. It follows that the number of particles per unit surface area, and hence the free energy cost of the interface, is smaller between the gas cloud and the liquid shadow than between the gas shadow and the liquid cloud.

## B. Critical point shifts

Here we enquire how the critical point parameters of the size disperse fluid depend on the degree of polydispersity  $\delta$ . To this end we have employed simulation to investigate four Schulz distribution with width parameters (cf. Eq. (3))  $z = 50, 25, 10$  and  $5$ , corresponding to polydispersities  $\delta = 14\%, 19.6\%, 30.1\%, 40.7\%$  respectively. For  $z = 5$  and  $z = 10$ , the size distribution was truncated at  $\sigma_c = 3.0$ , while for  $z = 25$  and  $z = 50$  a cutoff  $\sigma_c = 2.0$  was used.

Standard finite-size scaling (FSS) methods were used to estimate the location of the critical point in each case studied. The FSS methodology exploits the critical point scale invariance of the fluctuation spectrum of quantities such as the number density, as expressed through

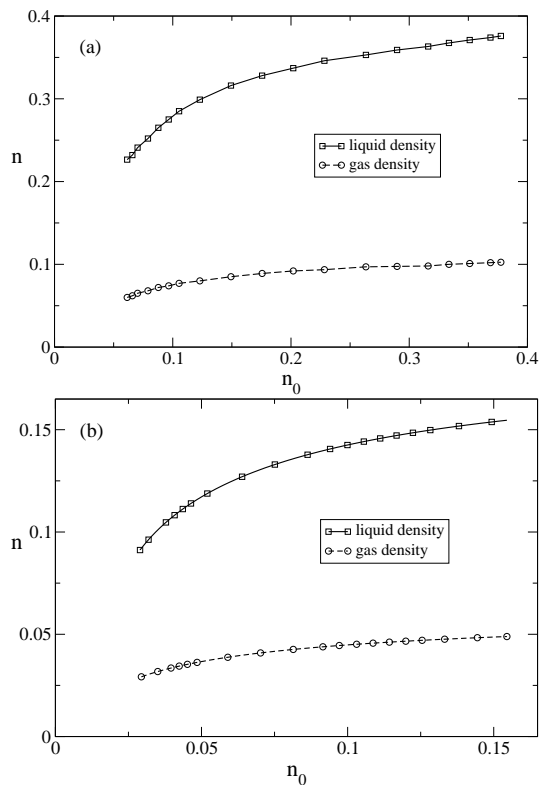


FIG. 8: Dependence of the gas and liquid densities on the overall parent number density  $n_0$ . **(a)** Simulation results extracted from fig. 7. **(b)** The corresponding results from the MFE calculations at  $t = 0.91t_c$ .

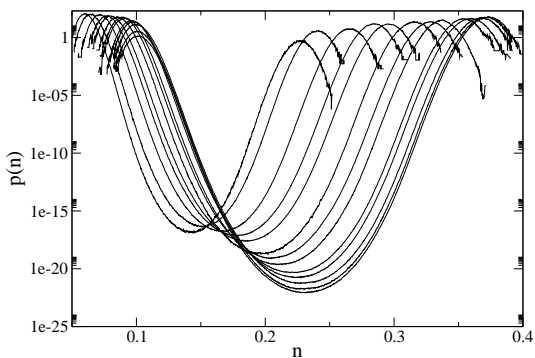


FIG. 9: The data of fig. 7 plotted on a logarithmic scale in order to expose the scale of the free energy barrier separating the pure phase gas and liquid states in the coexistence region.

the form of  $p(n)$  [28]. For the  $z = 50$  and  $z = 25$  distributions, three system volumes were studied, namely  $V = 3375\bar{\sigma}^3, 8000\bar{\sigma}^3, 15625\bar{\sigma}^3$ . For the  $z = 10$  and  $z = 5$  distributions, somewhat larger simulation cells were required, the values chosen being  $V = 11390\bar{\sigma}^3, 27000\bar{\sigma}^3$ , and  $V = 52734\bar{\sigma}^3$ . We note that the largest of these systems contained over  $10^4$  particles at criticality.

In order to compare with the simulation results, MFE calculations were performed to obtain the critical point for width parameters in the range from  $z = 1$  to the

monodisperse limit  $z = \infty$ . The resulting comparison is shown in fig. 10. We note that while the simulations were able to locate the critical temperature  $t_c$  rather accurately (the error bar is smaller than the symbol size), the estimates of the critical volume fraction  $\eta_c$  carry a rather large estimated error because of the difficulty in obtaining good statistics for large systems and high degree of polydispersity. Thus, although we find a strong increase in  $t_c$  with increasing  $\delta$ , no clear trend is observed for  $\eta_c$ . The MFE results confirm the increase of  $t_c$  with increasing  $\delta$ . However, the fractional change is substantially less than that observed in the simulations. As regards the critical volume fraction, the MFE method predicts a significant (5%) decrease in the value of  $\eta_c$  over the range of  $\delta$  studied in the simulations. The scale of this decrease is, however, larger than any that might be considered consistent with the simulation error bars.

### C. Location of the critical point

An important finding of our investigation of critical point shifts is that, for each  $z$  studied, the critical point occurs at, or very close to, the maximum of the cloud and shadow curves. Correspondingly, there is no numerical evidence of distinct cloud and shadow points at or above  $t_c$ , either in the simulations or the MFE calculations. This observation is consistent with earlier results obtained from a simpler model free energy [15], but clearly calls for an explanation: in a polydisperse system the critical point must be found at an intersection of the cloud and shadow curves, and this intersection will in general be located *below* the maxima of the two curves [11, 14].

One possible way to investigate when the critical point is near the top of the cloud (and hence also the shadow) curve is to find conditions under which the slope of the cloud curve there is zero. This can be done for simple excess free energies depending only on a single density moment, within the framework of a Landau expansion [14]. However, such an approach becomes excessively unwieldy when several density moments are involved. We have therefore addressed the question in a more indirect way. On general grounds the spinodal curve, where a given polydisperse phase becomes locally unstable, must lie inside the cloud curve and touch it at the critical point [11]. This implies that the critical point is at the maximum of the cloud curve exactly when it coincides with the maximum of the spinodal (as happens in monodisperse systems). We can therefore estimate the shift of the critical point away from the cloud curve maximum by comparing its location with that of the spinodal maximum: as long as these two points are close together, the critical point should also be close to the cloud curve maximum.

The advantage of this approach is that both the spinodal curve and the critical point can be calculated relatively easily within the MFE framework, from local properties of the excess free energy surface. Fig. 10

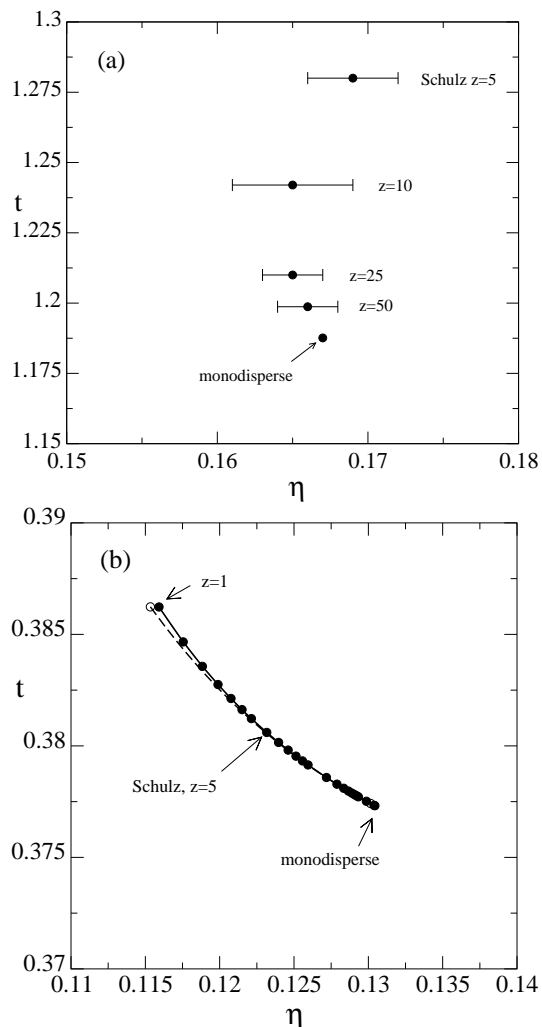


FIG. 10: (a) Simulation estimates of the critical temperature and volume fraction for Schulz parent distributions of a variety of widths (see text for details). (b) Corresponding predictions of the MFE calculations for Schulz distributions in the range  $z = 1$  to  $z = \infty$  (monodisperse limit). The dashed line and empty circle indicate the location of the spinodal maximum; see sec. V C.

shows that the resulting locations of the critical point and spinodal maximum are, though not identical, extremely close for the whole range of width parameters  $z$  studied above. Even for the most polydisperse system ( $z = 1$ ,  $\delta = 1/\sqrt{2} \approx 70\%$ ) the temperature coordinates of the two points are indistinguishable on the scale of the graph, confirming our earlier observation that the critical point is very near the cloud curve maximum.

To understand under which circumstances such rather unusual behaviour can be expected, we have derived general expressions for the location of the critical point and spinodal maximum in a polydisperse system with a smooth (van der Waals-type) excess free energy. Details will be given in a forthcoming publication [48]. Within an expansion valid for near-monodisperse systems, i.e.

small polydispersity  $\delta$ , the leading shifts in the critical point and spinodal maximum relative to the monodisperse limit  $\delta \rightarrow 0$  turn out to be  $O(\delta^2)$ . The density shifts are in general *different* as expected on general grounds for a polydisperse system; see above. (The temperature shifts, which are essentially quadratic in the density shifts because we are expanding around the maximum of the monodisperse spinodal curve, are always identical to  $O(\delta^2)$ .) However, it turns out that for purely size-polydisperse systems, where the excess free energy is unchanged if we scale all particle sizes and interparticle separations by the same factor, the lowest-order density shifts of critical point and spinodal maximum *exactly* coincide. Likewise, one can show using the techniques of [16, 47] that size polydispersity causes the lowest-order shifts in the entire cloud and shadow curves to be identical, once they are plotted in terms of volume fraction rather than density. This is consistent with our observation of the near-coincidence of these curves in fig. 2.

Thus the perturbative expansion shows that the effects which we observe numerically are due to the fact that our LJ system has purely size-polydisperse interactions. This rationalizes why earlier calculations [15] also found the critical point very near the top of the cloud curve, even though a much simpler free energy model was used: any excess free energy which respects the scale invariance of a size-polydisperse system will exhibit such behaviour.

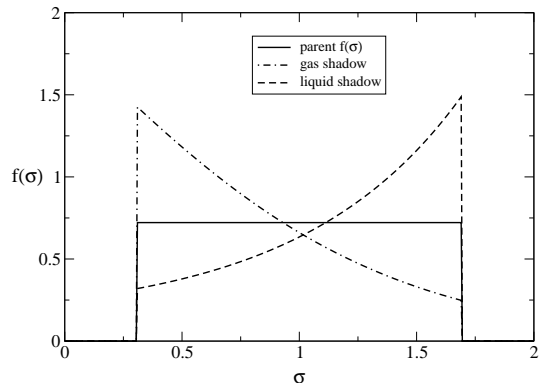


FIG. 11: Normalized size distributions in the daughter phases on the shadow curves at  $t \approx 0.9t_c$ , for a top hat parent distribution with polydispersity  $\delta = 40\%$ .

We initially thought that the fact that our critical points were at the top of the cloud curves was related to the size distributions in the shadow phases being essentially just scaled versions of the cloud (parent) size distributions; see fig. 5. Indeed, one can show that for any size-polydisperse excess free energy which depends only on the density moments  $\rho_0$  and  $\rho_1$ , this scaling holds *exactly* when the parent phase has a Schulz size distribution [48]. In such a scenario the cloud and shadow curves also coincide exactly in the  $\eta - t$  representation, and the critical point is exactly at their common maximum [48]. However, the same features can occur, to a very good approximation, even when there is no scaling

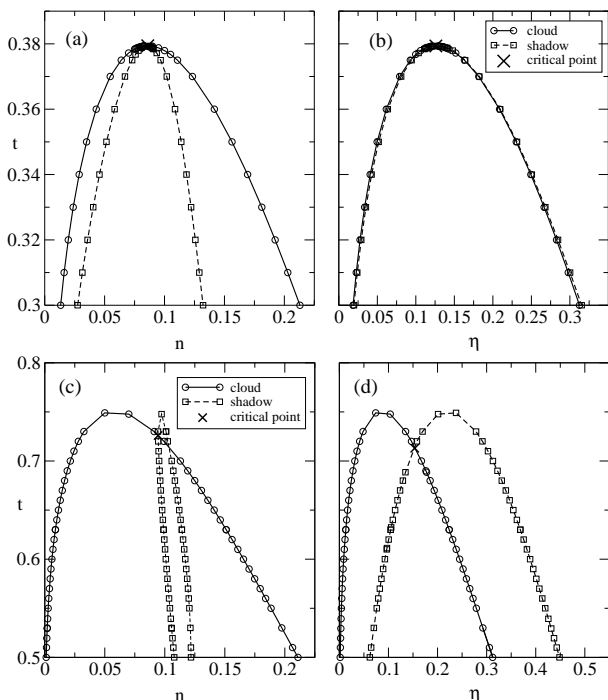


FIG. 12: **(a,b)** Cloud and shadow curves in the  $n - t$  and  $\eta - t$  planes, for a parent with a top-hat size distribution, as obtained by MFE calculations. **(c,d)** The analogous results for a system with added amplitude polydispersity; the critical point is now clearly below the maximum of cloud and shadow curves.

link between cloud and shadow size distributions. We demonstrate this by considering theoretically a parent phase with a top hat size distribution, with the polydispersity  $\delta = 40\%$  taken to be the same as our main Schulz distribution example. Fig. 11 shows exemplary size distributions in the shadow phases: these are now clearly different in shape from each other and from the parent. Nevertheless (fig. 12(a,b)) the  $\eta - T$  cloud and shadow curves are almost identical and the critical point is extremely close to their maximum.

Finally, the above theoretical arguments suggest that, once we move to a case where polydispersity affects not only the size but also the amplitude of the interaction potentials, the behaviour expected for a generic polydisperse system should be recovered. To confirm this, we repeated the MFE calculations for interaction potentials  $U_{ij}$ , Eq. (5), scaling as the product  $\sigma_i \sigma_j$  of the sizes of the particles involved. This translates into an additional factor  $\sigma \sigma'$  in the attractive term in the model free energy (Eq. 7). The results are shown in fig. 12(c,d) for the top hat parent: as expected, the critical point is now clearly below the cloud curve maximum, and the  $\eta - T$  representations of the cloud and shadow curves no longer coincide. Preliminary simulation results for a LJ model with combined size and amplitude polydispersity confirm this scenario [49].

## VI. DISCUSSION AND OUTLOOK

In summary, we have used specialized MC simulation and the moment free energy (MFE) method to study the liquid-gas phase behaviour of a size-disperse LJ fluid having a degree of polydispersity  $\delta = 40.7\%$ . Cloud and shadow curves have been traced and fractionation effects quantified. Surprisingly good qualitative agreement is found in almost all aspects of the results between the simulations and the MFE calculations for a van der Waals model.

In a related study, we have also obtained the dependence of the critical point parameters on the degree of polydispersity. The simulation show a strong rise in the critical temperature with increasing  $\delta$ , but no clear trend in the critical volume fraction  $\eta_c$ . The increase in  $t_c$  is confirmed by the MFE calculation, albeit with a weaker magnitude. However, in contrast to the simulation, the MFE predicts quite a strong decrease of  $\eta_c$  with increasing  $\delta$ .

Some of our findings for the sub-critical coexistence region seemed, at first sight, rather surprising: the cloud and shadow curves nearly collapsed onto a common curve in the  $\eta - t$  representation, with the critical point found so close to their maximum as to be indistinguishable. We outlined a theoretical argument which shows that such behaviour is generically to be expected for systems with pure size-polydispersity, but not otherwise. This was confirmed by, on the one hand, considering a different parent size distribution, with a top hat shape: similar behaviour was observed. The addition of amplitude polydispersity, on the other hand, completely changed the picture. We demonstrated finally that the close similarity in the shapes of the size distributions of cloud and shadow phases is rather peculiar to parents with a Schulz size distribution, and not directly linked to the occurrence of the other effects of size polydispersity which we observe.

Given the rather crude nature of the van der Waals free energy Eq. (8), used for the MFE calculation, the level of qualitative agreement with the simulations in the sub-critical region is gratifying. We note, however, that previous work treating polydispersity within a van der Waals framework [15] did not produce a similar level of agreement. We tentatively ascribe this difference to the inclusion in the present work of an explicitly polydisperse hard-core reference free energy having the well known BMCSL form [36, 37]. Use of this reference free energy improves the description of packing effects. These are expected to be particularly important for the correct description of liquid structure in polydisperse fluid because of the possibility that small particles can fit into the gaps between large ones. We speculate that it is this ability to pack more effectively (and the resulting lowering of the configurational energy) which is responsible for the observed increase in  $t_c$  with increasing polydispersity, a finding which contrasts with the predicted *decrease* in ref. [15].

One surprise arising from the simulation results is the observed magnitude of coexistence curve broadening. In simulations of a monodisperse system at coexistence, the system fluctuates freely between both phases (assuming the provision of an appropriate multicanonical weight function) [28]. The form of  $p(n)$  exhibits two peaks, and these are visible over a certain range of  $\mu$  due to finite-size smearing of the transition. By contrast the range of  $\mu(\sigma)$  (fig. 4) over which gas and liquid phase peaks are visible (cf. fig. 7) is 1-2 orders of magnitude greater than the finite-size smearing one would expect in a monodisperse system having a similar number of particles. Consequently a large number of separate, but overlapping (in configuration space) simulations are required to bridge the coexistence region from pure gas to pure liquid.

With regard to the general simulation issues raised in this study, we have shown that recently developed techniques (dilution line tracking [31] bootstrapped by the non-equilibrium potential refinement method [32]) can be successfully employed to map the phase behaviour of fluids exhibiting fixed polydispersity. This is achieved within what is arguable the most flexible framework for the study of fluid phase equilibria, namely the grand canonical ensemble. Notwithstanding these advances, however, it should be stressed that the simulations themselves are not yet routine: the work reported here consumed well over  $10^4$  hours of CPU time on a 2 GHz PC processor. Such an investment of effort exceeds that necessary for obtaining the phase behaviour of a monodisperse fluid by a factor of 1-2 orders of magnitude.

The source of the computational complexity is twofold. Firstly, one needs to utilize system sizes whose linear extent exceeds a given factor of the largest possible particle diameter. Even for moderate polydispersities, this can increase the necessary volume by an order of magnitude compared to the monodisperse case. Secondly, in order to relax the system between sampled configurations, one must decorrelate not only the overall density, but also the distribution of particle sizes  $\rho(\sigma)$ . The bottleneck for the latter process is the largest particles, for which the probability of particle insertions and deletion is small, and which can thus only be altered by the resizing moves whose effect is generally more incremental in magnitude. Clearly there is scope for further algorithmic improvements in this regard.

As an extension of the present study, work is under way to simulate the phase diagram of a Lennard-Jones fluid in which the well depth in the LJ interaction potential depends on the sizes of the interacting particles. Preliminary results [49] confirm the prediction of the MFE calculations described in sec. VC, i.e. that the cloud and shadow curves adopt the standard order and that the critical point lies well below the extremum of the cloud and shadow curves.

#### Acknowledgments

The authors acknowledge support of the EPSRC, grant numbers GR/S59208/01 and GR/R52121/01.

- 
- [1] J.J. Salacuse and G. Stell, *J. Chem. Phys.* **77**, 3714 (1982).
- [2] D. A. Kofke and E.D. Glandt, *J. Chem. Phys.* **87**, 4881 (1987).
- [3] J.N. Israelachvili, D.J. Mitchell and B.W. Ninham, *J. Chem. Soc. Faraday Trans* **272**, 1526 (1976).
- [4] M.J. Grimson and F. Honary, *Phys. Lett.* **102A**, 241 (1984).
- [5] E. Dickinson, *Phys. Rev. Lett.* **53**, 728 (1984).
- [6] G.C. Barker and M.J. Grimson, *Mol. Phys.* **63**, 145 (1988).
- [7] R. Blaak and J.A. Cuesta, *J. Chem. Phys.* **115**, 963 (2001).
- [8] W.B. Russel, D.A. Saville and W.R. Schowalter, *Colloidal Dispersions*, (Cambridge U.P., Cambridge, 1989).
- [9] G.J. Vrooje and H.N.W. Lekkerkerker, *J. Chem. Phys.* **97**, 3601 (1993).
- [10] A. Nesarikar, M. Olvera de la Cruz and B. Crist, *J. Chem. Phys.* **98**, 7385 (1993).
- [11] For a review see: P. Sollich, *J. Phys. Condens. Matter* **14**, R79 (2002).
- [12] P. Sollich, P.B. Warren and M.E. Cates, *Adv. Chem. Phys.* **116**, 265 (2001).
- [13] K. Ghosh and M. Muthukumar, *Phys. Rev. Lett.* **91**, 158303 (2003).
- [14] C. Rascón and M.E. Cates, *J. Chem. Phys.* **118**, 4312 (2003).
- [15] L. Bellier-Castella, H. Xu and M. Baus, *J. Chem. Phys.* **113**, 8337 (2000).
- [16] R.M.L. Evans, D.J. Fairhurst and W.C.K. Poon, *Phys. Rev. Lett.* **81**, 1326 (1998).
- [17] A. van Heukelum, G.T. Barkema, M.W. Edelman, E. van der Linden, E.H.A de Hoog, R.H. Tromp, *Macromolecules* **36**, 6662 (2003).
- [18] D. J. Fairhurst and R. M. L. Evans, *Colloid & Polymer Science* (in press)
- [19] P.G. Bolhuis and D.A. Kofke, *Phys. Rev.* **E54**, 634 (1996); D.A. Kofke and P.G. Bolhuis, *Phys. Rev.* **E59**, 618 (1999).
- [20] M.R. Stapleton, D.J. Tildesley, N. Quirke; *J. Chem. Phys.* **92**, 4456 (1990)
- [21] D. A. Kofke; *J. Chem. Phys.* **98**, 4149 (1993).
- [22] T. Kristóf and J Liszi, *Mol. Phys.* **99**, 167 (2001).
- [23] J.A. Gualtieri, J.M. Kincaid and G. Morrison, *J. Chem. Phys.* **77**, 521 (1982).
- [24] H. Xu and M. Baus, *Phys. Rev.* **E61**, 3249 (2000).
- [25] M. Fasolo and P. Sollich, *Phys. Rev. Lett.* **91**, 068301 (2003).
- [26] A short report on some aspects of this study has previously appeared elsewhere: N.B. Wilding and P. Sollich, *Europhys. Lett.* (in press); cond-mat/0403391.
- [27] See e.g. S.-E. Phan, W.B. Russel, J. Zhu and P.M. Chaikin, *J. Chem. Phys.* **108**, 9789 (1998).
- [28] N.B. Wilding, *Phys. Rev.* **E52**, 602 (1995).

- [29] A.Z. Panagiotopoulos; J. Phys. Condens. Matter **12**, R25 (2000).
- [30] N.B. Wilding; Am. J. Phys. **69**, 1147 (2001).
- [31] N.B. Wilding and P. Sollich, J. Chem. Phys. **116**, 7116 (2002). See also F. Escobedo, J. Chem. Phys. **115**, 5642 (2001); *ibid* **115**, 5653 (2001).
- [32] N.B. Wilding; J. Chem. Phys. **119**, 12163 (2003)
- [33] A.M. Ferrenberg and R.H. Swendsen; Phys. Rev. Lett. **63**, 1195 (1989).
- [34] A.D. Bruce and N.B. Wilding; Adv. Chem. Phys. **127**, 1 (2003).
- [35] B. Berg and T. Neuhaus, Phys. Rev. Lett **68**, 9 (1992).
- [36] T. Boublík, J. Chem. Phys. **53**, 471 (1970).
- [37] G.A. Mansoori, N.F. Carnahan, K.E. Starling, T.W. Leland, J. Chem. Phys. **54**, 1523 (1971).
- [38] N. F. Carnahan, K. E. Starling, J. Chem. Phys. **51**, 635, (1969)
- [39] P. Sollich and M.E. Cates, Phys. Rev. Lett. **80**, 1365 (1998)
- [40] P.B. Warren, Phys. Rev. Lett. **80**, 1369 (1998).
- [41] N. Clarke, J.A. Cuesta, R. Sear, P. Sollich, and A. Speranza. J. Chem. Phys., **113**, 5817 (2000).
- [42] A. Speranza and P. Sollich, J. Chem. Phys., **117**, 5421 (2002).
- [43] A. Speranza and P. Sollich, J. Chem. Phys. **118**, 5213 (2003).
- [44] I. Pagonabarraga and M.E. Cates, Europhys. Lett. **55**, 348 (2001).
- [45] Our terminology here is to refer to the liquid phase which is the shadow coexisting with the gas phase at its cloud point as the “liquid shadow”, and conversely for the gas shadow. This emphasizes the physical nature of the various phases. One could alternatively define the liquid shadow to be shadow phase *of* a liquid at its cloud point; this would then be a gas phase. The latter convention is the one adopted in [26].
- [46] K. Binder, Phys. Rev. **A25**, 1699 (1982).
- [47] R.M.L. Evans, Phys. Rev. **E59** 3192 (1999); J. Chem. Phys. **114**, 1915 (2001).
- [48] P. Sollich, unpublished.
- [49] N.B. Wilding, unpublished data.